metals

MDPI

Article

Morphology Control of Metal Pool and Eutectic Carbides in Electroslag Remelted M2 HSS with an External Axial Static Magnetic Field

Xuhui Zhao [1,2], Zhonghao Sun [1,2], Zhibin Xia [1,2], Chunmei Liu [1,2], Zhe Shen [1,2], Biao Ding [1,2], Tianxiang Zheng [1,2], Yifeng Guo [1,2,*], Qiang Li [1,2,*] and Yunbo Zhong [1,2,*]

[1] State Key Laboratory of Advanced Special Steel, Shanghai University, Shanghai 200444, China
[2] School of Materials Science and Engineering, Shanghai University, Shanghai 200444, China
* Correspondence: yfguo@shu.edu.cn (Y.G.); liqiangshu@shu.edu.cn (Q.L.); yunboz@staff.shu.edu.cn (Y.Z.)

Abstract: This study investigates the influence of a superimposed axial static magnetic field (ASMF) on the morphology of metal pool and eutectic carbides (ECs) in electroslag remelted M2 high-speed steel (HSS). The application of ASMF caused the metal pool to become shallower, and the solidified structure to expand axially, along with finer (i.e., more uniformly distributed and crystallographically oriented) ECs. Lorentz force-driven unidirectional circulation in slag pool was the primary cause of the metal pool's morphological adjustment; this resulted in a more homogenous temperature distribution in slag pool. Thus, the heat transfer from the slag pool to the metal pool became more uniform, creating a metal pool that is shallower. Additionally, local solidification time (LST) became shorter, while the number of (Ti, V)N-Al_2O_3 inclusions serving as heterogeneous nuclei for EC formation increased due to ASMF, enabling finer EC with more crystallographic orientations in ESR ingots.

Keywords: M2 HSS; ESR; ASMF; metal pool; ECs

check for updates

Citation: Zhao, X.; Sun, Z.; Xia, Z.; Liu, C.; Shen, Z.; Ding, B.; Zheng, T.; Guo, Y.; Li, Q.; Zhong, Y. Morphology Control of Metal Pool and Eutectic Carbides in Electroslag Remelted M2 HSS with an External Axial Static Magnetic Field. *Metals* **2023**, *13*, 912. https://doi.org/10.3390/met13050912

Academic Editor: Andreas Chrysanthou

Received: 9 April 2023
Revised: 29 April 2023
Accepted: 6 May 2023
Published: 8 May 2023

Copyright: © 2023 by the authors. Licensee MDPI, Basel, Switzerland. This article is an open access article distributed under the terms and conditions of the Creative Commons Attribution (CC BY) license (https://creativecommons.org/licenses/by/4.0/).

1. Introduction

AISI M2 steel is known by many as one of the most widely used high-speed steels (HSSs) with high hardness and wear resistance [1]. This steel's hot hardness is accomplished by incorporating a substantial quantity of carbides into its microstructure, and the uniform distribution of these fine carbides is crucial to its performance [2–7]. Nonetheless, considering its high alloy and carbon content and inevitable severe segregation, undesirable ECs (typically distributed unevenly and coarse) are formed in the interdendritic region during the solidification process of this steel [8,9], particularly in the case of larger ingots.

Increasing the cooling rate during solidification is the most effective method to reduce elemental segregation and modify the carbides [10–12]. Electroslag remelting (ESR), thus, is believed to be effective in modulating the segregation and microstructure of high alloyed steel (such as M2 HSS) because of the water-cooled mold and baseplate compared with the traditional die casting [13–19]. Nevertheless, with increasing ESR ingot diameter, the cooling capacity of the baseplate and mold progressively decreases. The cooling effect is insufficient, particularly in the ESR ingot's core, while the metal pool's depth increases [20,21]. Consequently, segregation and other metal metallurgical defects, as well as coarse ECs, tend to happen for large M2 HSS ESR ingots, a problem that has yet to be resolved in the industrial sector.

Metallurgists have made numerous efforts from different perspectives to solve the appeal problem. One effort is micro-alloying (including rare earth) and modification method. Liu et al. [22] and Yin et al. [23] added 0.3 wt.% of Ce-La to the ESR process and discovered that adding Ce-La could help alter the type of inclusions, thereby refining the solidified structure as having heterogeneous nuclei. The degree of elemental segregation

between dendrites was reduced, eliminating ECs with network morphology. Nonetheless, if the addition procedure is not strictly regulated, the addition of these rare earth elements or their composites will result in an asymmetrical distribution within the ESR ingot and may introduce undesirable contaminants [23]. The ESR process's power supply conditions (e.g., melting current, frequency, voltage) are also being optimized. Du et al. [24] and Yu et al. [25] proposed that a shallower metal pool can be obtained by employing a lower melting current in the ESR process, which results in refining the primary carbide. However, at lower melting currents, the surface quality of ESR ingots deteriorates, and productivity is also impacted. Moreover, Chang et al. [26] applied low-frequency alternating current (AC) power in ESR. They discovered that the metal pool becomes flatter, thereby refining the solidified structure of the alloy. At the same time, the oxygen content in the ingot increases due to the inevitable electrolytic reactions during low-frequency ESR. The final effort focuses on restructuring and redesigning the ESR device. Based on the conventional ESR process, Cao et al. [27] put forward a "single power two circuits" design; as a consequence, the temperature distribution in a metal pool becomes more uniform (flatter and shallower), which facilitates the development of finer microstructure. Other designs such as mold/electrode rotation [28–30] and electroslag continuous casting (ESCC) [31–34] refined the microstructure of ESR ingots by controlling the metal slag pool's morphology, described in relevant literature above.

Recently, the external static magnetic field (MF) has been introduced to regulate ESR solidification, denoted as magnetic-controlled (MC)-ESR [35]. Compared to the imposed alternating MF (electromagnetic stirring) or pulsed MF on the ESR process proposed by other researchers [36,37], because skin effect (due to the water-cooled mold) tends to happen with the application of alternating or cyclic MF, there is a significant benefit for static MF. Such technology is currently being investigated for a variety of steel grades including low-alloyed GCr15 bearing steel [38,39], medium-alloyed H13 die steel [40,41], and high-alloyed M2 HSS [42,43]. Guo et al. [42,43] applied a transverse static MF (TSMF, with different magnetic flux densities) for regulating M2 HSS solidification upon ESR. The depth of the metal pool in the ESR ingot decreased after applying the TSMF, and the coarse net-like morphology of the ECs almost disappeared. It has been shown that the ECs of M2 HSS can be refined by superimposing the TSMF on the ESR process. Nevertheless, due to the fact that two permanent NdFeB magnets generated TSMF (positioned outside the mold) in our previous work, the magnetic flux density (MFD) of large-scale ESR ingots would decline significantly. In addition, the TSMF was unidirectional (asymmetry), which may also lead to uneven macrostructure in larger ESR ingots.

To solve the above problems, an axial static MF (ASMF, axisymmetric) was proposed in this study. The goal of this article is to investigate the evolution law of the metal pool/ECs' morphology under the action of applied ASMF. Initially, the metal pool's solid-liquid interface and ECs in ESR ingots were observed. The size distribution and fractional area of ECs in ESR ingots were then detected and quantified in detail. To evaluate 50 mT ASMF's effect on the M2 HSS ESR ingot's homogeneity enhancement, its hardness uniformity was also measured. By clarifying the two mechanisms (shallower metal pool and finer ECs) due to ASMF, the current study sheds new light on the preparation of high homogeneous M2 HSS.

2. Experimentation

2.1. Material and Procedure

M2 HSS chemical compositions are shown in Table 1; the dimensions of the consumable electrodes used in this investigation were φ30 mm × 850 mm.

Table 1. HSS used in this study (mass percentage, %).

C	W	Mo	Cr	V	Si	Mn	Cu	Ni	S	P
0.84	5.7	4.64	4.12	1.84	0.36	0.36	0.1	0.09	0.005	0.025

The MC-ESR investigations were conducted in the open air, and Figure 1a depicts the apparatus that this study used. To prevent the mold exterior's magnetic screening, the mold (60 mm inner diameter) was made of copper internally and 304 stainless steel pipe externally. During MC-ESR, the cooling water discharge rate (20 °C) to the mold or baseplate was 800 L/h. The ASMF was produced by positioning energized copper coils (MF generator in Figure 1a) outside the mold and modifying the direct current (DC) in the copper coil. In addition, to observe the motion characteristics of the liquid slag, a camera was placed above the water-cooled mold to record, as shown in Figure 1a.

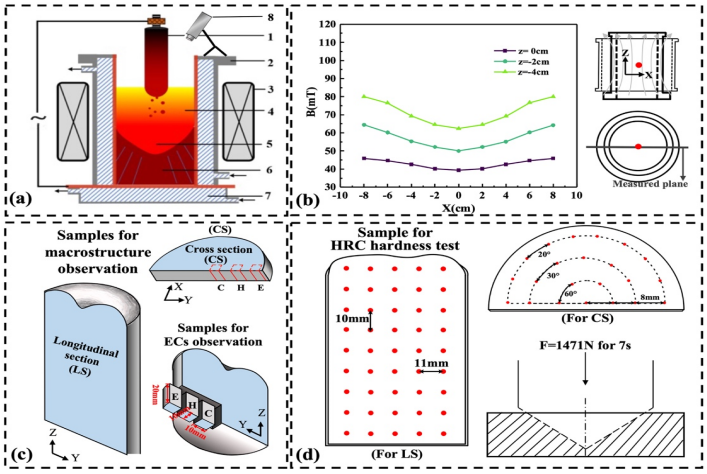


Figure 1. (**a**) Schematic illustration of the apparatus (1 electrode, 2 water−cooled mold, 3 MF generator, 4 slag pool, 5 metal pool, 6 ESR ingot, 7 water−cooled baseplate, 8 camera). (**b**) Distribution of the MFD of the ASMF along the ZX plane (26 A DC). (**c**) Schematic diagram of sampling method for macrostructure/ECs observation. (**d**) Schematic diagram for hardness test.

In this study, DC was set to 26 A, and Figure 1b shows the distribution of the MFD of the ASMF along the ZX plane (measured plane, central longitudinal section of mold or electrode). We maintained the stability of the remelting current via regulating the electrode's lowering velocity during remelting. In addition, the height of the mold's central cross-section was −2 cm (Z) in Figure 1b during the remelting process, which corresponds to a value of 50 mT for the MFD at the cross-section's center (red point in Figure 1b). The MFD of applied ASMF was measured by a Teslameter (HT201). In the remelting process, 60% CaF_2-20% CaO-20% Al_2O_3 slag mixtures (150 g) were chosen. In order to demonstrate the morphology of the metal pool, 60 g of Sn particulates with a low melting point was uniformly introduced in the slag pool during stable remelting. Simultaneously, 350 mm of the electrode was melted. In this investigation, a succession of experiments were conducted with various remelting currents (500 A, 600 A and 700 A) at 50 Hz and MFD (0 mT/50 mT). The total time for the remelting process (without ASMF) were 13.4 min (500 A), 12.1 min (600 A) and 10.3 min (700 A), corresponding to the remelting rate of 2.658 g/s, 2.975 g/s and 3.483 g/s, respectively. After applying the 50 mT ASMF, the total remelting time became 12.1 min (500 A), 10.1 min (600 A) and 9.1 min (700 A), corresponding to the remelting rate of 2.961 g/s, 3.575 g/s and 3.964 g/s, respectively. It can be seen that after the ASMF was applied, the total melting time was shortened, while the remelting rate was slightly increased.

2.2. Macrostructure/ECs Observation and Hardness Test

As depicted in Figure 1c, we cut the obtained M2 HSS ESR ingots (φ60 mm × 100 mm) at the center of the longitudinal section (LS) and cross section (CS) following the remelting process. Under various experimental conditions, we polished the cutting planes (blue planes in Figure 1c) and etched them for 120 s using a 5 g $FeCl_3$-10 mL HCl-90 mL CH_3CH_2OH solution (120 s) to disclose the macrostructures and solid–liquid interfaces (metal pool).

To observe ECs in different regions (ESR ingot), we selected three samples with dimensions of $10 \times 10 \times 20$ mm^3 at the ESR ingot's half-radius (H), edge (E), and center (C) regions. After polishing (the blue planes in Figure 1c), the ECs were observed in several locations of the ESR ingot using the backscattered electron (BSE) mode of the VEGA 3 easy probe scan electron microscope (SEM, TESCAN). The deeply etched sample (5% HF/95.5% H_2O_2 solution) was used for the energy dispersive spectrum (EDS) analysis of ECs. The area fraction (different regions under different experimental conditions) and size distribution (C region under 600 A condition with or without ASMF) of the ECs were then counted and statistically analyzed using the Image J software. Ten images (1000 times, SEM results) were selected randomly in the statistical process and ECs of various geometric forms were simplified into circles (equivalent diameter) when calculating their size. Using a ZEISS GeminiSEM 300 equipped with an Oxford detector and operating at 20 kev with the sample tilted at 70°, an electron backscatter diffraction (EBSD) was used to characterize the crystallographic orientation of each EC.

Under various experimental conditions, we assessed the Rockwell hardness (HRC) uniformity of the M2 HSS ESR ingot to determine the influence of 50 mT ASMF on the homogeneity improvement. The experiment was conducted using a macrohardness tester (HBRVU-187.5); the indenter was a diamond with 1471 N applied (for 7 s). Hardness values were measured at different LS (45) and CS (22) locations to obtain the hardness distribution across the entire section, as shown in Figure 1d.

3. Results and Discussion

3.1. Shallower Metal Pool and Mechanisms

Macrostructures of the ESR ingot (LS) under different experimental conditions (500 A, 600 A, and 700 A, with or without ASMF) are shown in Figure 2, where the columnar grain organization (along with their growth direction) can be seen. On the LS, the gray dashed lines denote the location of the CS samples, while the white dashed lines represent the metal pool's solid–liquid interfaces. The columnar grain growth direction (red arrows in Figure 2) was nearly perpendicular to these interfaces. Additionally, metal pools' morphology (depth, width) and grain growth angle (GGA) vary significantly under various experimental parameters.

As depicted in Figure 3a, we designate the depth/width of the metal pool as well as the GGA to reflect the aforementioned alterations. The width is defined as the full width at half maximum of the interface. The GGA is the angle between the longitudinal axis of the ESR ingot and the direction of grain growth. Ten positions (blue circles in Figure 3a) on the solid–liquid interfaces were chosen to reduce counting errors when calculating the average GGA. As the remelting current increases, the metal pool's depth/width and the average GGA increase, as depicted in Figure 3b (from 500 A to 700 A, regardless of ASMF presence). For instance, without ASMF, the metal pools' average depths were 32.08 mm for 500 A, 38.18 mm for 600 A and 42.60 mm for 700 A. The application of 50 mT ASMF reduced these values to 20.65 mm, 25.97 mm, and 27.66 mm, respectively. However, after the administration of ASMF, the metal pool's width expanded (31.69 mm to 38.05 mm for 500 A, 33.77 mm to 39.09 mm for 600 A, and 34.55 mm to 41.69 mm for 700 A), as shown in Figure 3b. Therefore, the addition of 50 mT ASMF caused the metal pool to become shallower. In addition, the average GGA decreased (50.09° to 37.28° for 500 A, 52.67° to 41.62° for 600 A, and 55.33° to 44.08° for 700 A), signifying that the ASMF facilitated the axial growth of columnar grains. Notably, the central region (highlighted in yellow) of the ESR ingot (LS) contains a region of nearly axially grown grains (NAGG, defined as GGA with less than 15°), as depicted in Figure 2. The width of the NAGG is also measured in Figure 3b, and the values increase after the application of the ASMF (9.78 mm to 13.48 mm for 500 A, 10.87 mm to 14.65 mm for 600 A and 11.85 mm to 16.50 mm for 700 A).

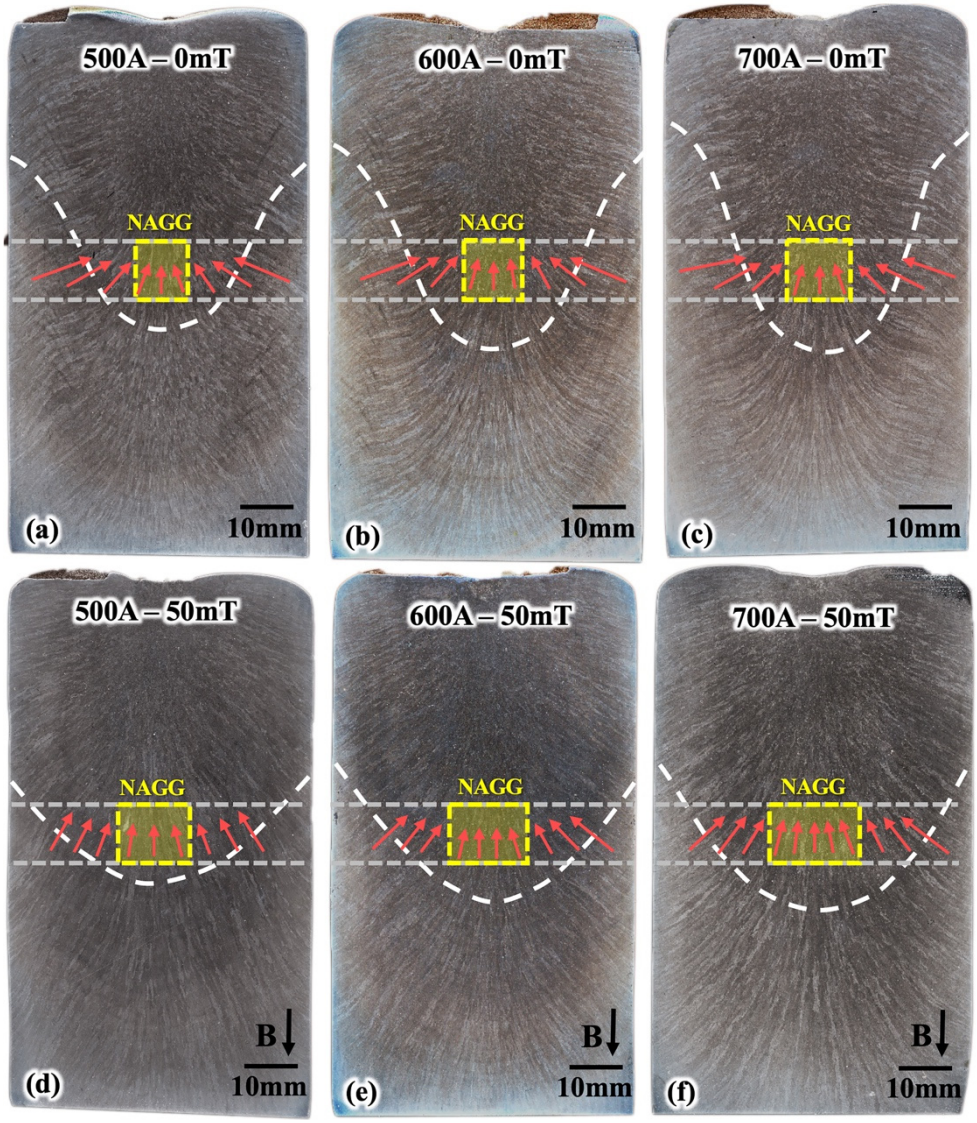


Figure 2. Macrostructures of the ESR ingot (LS) under different experimental conditions, (**a**) 500 A 0 mT, (**b**) 600 A 0 mT, (**c**) 700 A 0 mT, (**d**) 500 A 50 mT, (**e**) 600 A 50 mT, (**f**) 700 A 50 mT, respectively.

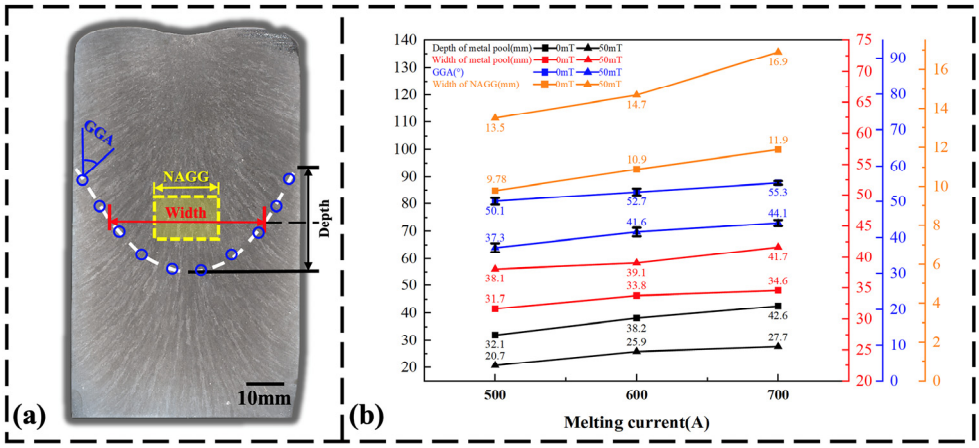


Figure 3. (**a**) Definition of the width/depth of metal pool and the GGA/NAGG. (**b**) The corresponding measurement results under different experimental conditions.

Figure 4 illustrates the macrostructures of an ESR ingot (CS) under various experimental parameters (500 A, 600 A and 700 A, with or without 50 mT ASMF). Without ASMF, a relatively fine-grained (RFG) region (highlighted in yellow) was present in the ESR ingot's center, which was encompassed by columnar grain morphology (Figure 4a,c,e). The area component of the RFG is 16.7% (500 A, 0 mT), 19.0% (600 A, 0 mT) and 21.1% (700 A, 0 mT). The RFG was distributed over the entire CS and the developed columnar grain morphology nearly disappeared after applying ASMF, as depicted in Figure 4b,d,f.

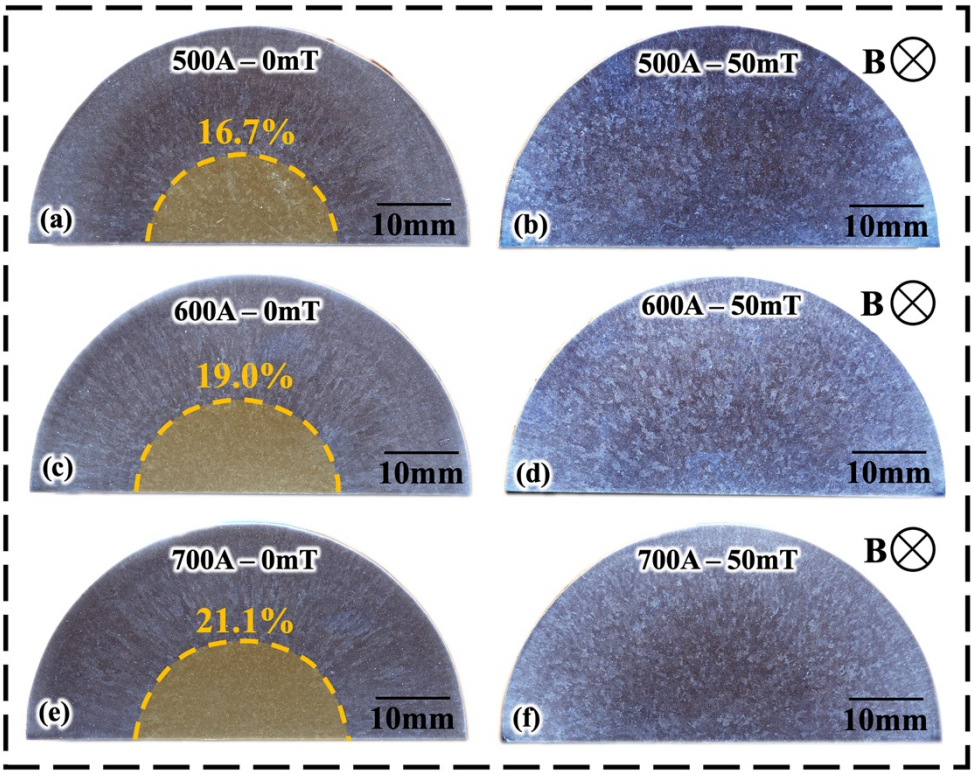


Figure 4. Macrostructures of the ESR ingot (CS) under different experimental conditions, (**a**) 500 A 0 mT, (**b**) 500 A 50 mT, (**c**) 600 A 0 mT, (**d**) 600 A 50 mT, (**e**) 700 A 0 mT, (**f**) 700 A 50 mT, respectively.

After applying the ASMF, the flow characteristics of the melt in the slag pool changed. In the absence of ASMF, the melt was shown as an up-and-down tumbling state. However, after the ASMF was implemented, the melt flow characteristics changed to a unidirectional circulating state (for details, please refer to Supplementary Videos S1 and S2 (600 A with or without ASMF)).

During steady-state remelting, the primary Joule heat source in the ESR ingot's metal pool is heat transfer from liquid slag and droplets. Figure 5 depicts this study's schematic diagram of the heat transfer and solidification process for different experimental conditions (with or without ASMF). Cao et al. [27] pointed that the temperature distribution of the slag pool (above the metal pool) has a substantial impact on the morphology and temperature distribution of the metal pool. In a typical ESR (without ASMF), the high-temperature region was located in the center of the slag pool, and the slag near the mold is subjected to an intensive quenching effect of cooling water, resulting in increased heat transfer to the center of the metal pool, as illustrated in Figure 5a (Q_1). Moreover, due to the smaller size of the electrode applied in this study, the droplet shows a single drop at the center of the electrode end [44]. As a consequence, the temperature distribution is inhomogeneous, while the shape resembled a pointed "V" in the metal pool. As the remelting current increases (from 500 A to 700 A), more Joule heat is produced due to the greater current traveling through the liquid slag [45]. As depicted in Figures 2a–c and 3b, the inhomogeneity of the metal pool's temperature distribution grows, resulting in a deeper metal pool.

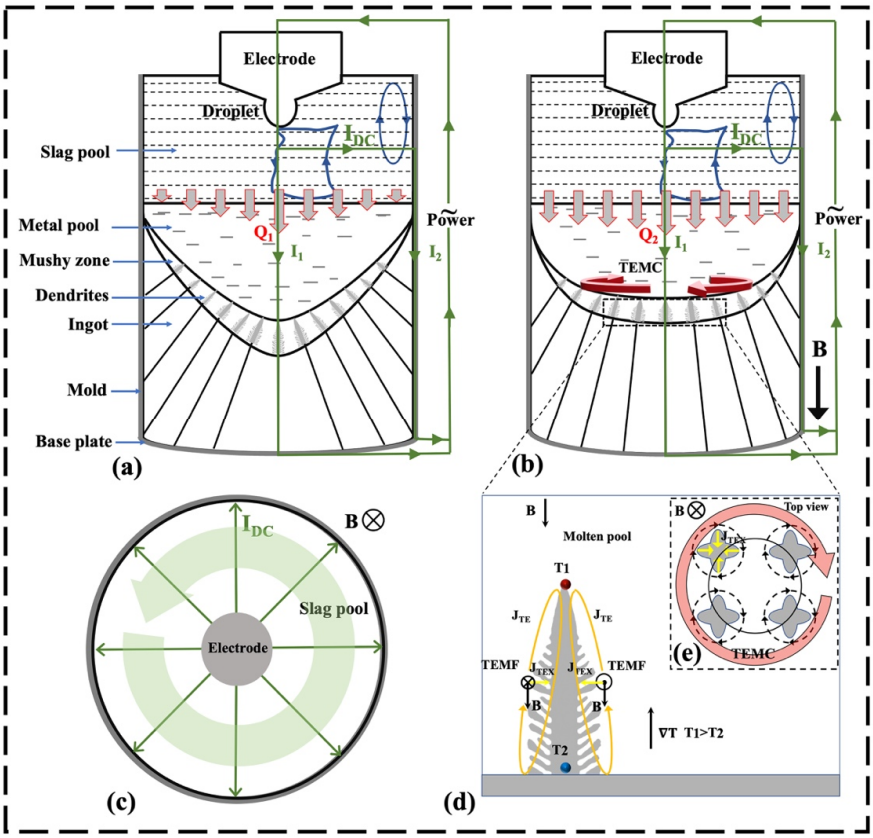


Figure 5. Schematic diagram of the heat transfer and solidification process for different experimental conditions (with or without ASMF) in this study. (**a**) Without ASMF, (**b**) With ASMF, (**c**) Unidirectional Lorentz force-driven lateral circulating flow (unidirectional) in slag pool (top view) due to ASMF, (**d**) Mechanism of TEMC formation and (**e**) Macroscopic unidirectional TEMC at the solid-liquid interface (top view) due to ASMF, respectively.

Wang et al. [45] discovered two pairs of vertical flows in the slag pool in the traditional ESR process. The heat from the cooling water causes the slag to descend near the lateral wall, resulting in a steady circulation in a clockwise direction. In the meantime, the descending droplets at the center of the liquid slag produces a counterclockwise flow (blue circles in Figure 5a,b). These factors lead to the up-and-down tumbling state of the melt in the slag pool without applying the ASMF, as shown in the Supplementary Video S1. Since there is no insulation between the mold and the base plate during the ESR process, the current has two loops in the overall melting system [46]. As illustrated in Figure 5a,b (green lines), one loop is "power—electrode—slag pool—metal pool—ingot—base plate—power", called the ingot circuit (I_1). The other loop is "power—electrode—slag pool—mold—base plate—power", called the mold circuit (I_2). Li [47] recorded the current signal during the ESR process with a 50 Hz remelting current and noted the existence of a DC component (I_{DC}) in the mold circuit, the magnitude of which is between 8% and 15% of the AC component in the I_2 circuit (Figure 5a,b). In this instance, the externally applied ASMF will interact with the I_{DC} to generate Lorentz force, which inevitably has an additional effect on the flow characteristics of the slag pool. An approximate calculation is performed here to determine the effect of Lorentz force (F_L, generated by I_{DC} and applied ASMF) on the slag pool's flow characteristics in this study. According to previous literature [46], the DC component of the current (I_{DC}) is about 2% of the peak current value (I total) when the filling ratio of ESR process is 0.5. The current density (J) of I_{DC} can be determined easily, and is equal to $I_{total} \times 0.02/S$ electrode, where S electrode refers to the cross-sectional area of the electrode. For different remelting conditions, the values of J calculated are 1.42×104 A/m^2 (500 A), 1.70×104 A/m^2 (600 A) and 1.98×104 A/m^2 (700 A), respectively. Then, F_L ($F_L = J \times$ B,

B is the MFD) are about 710 N/m^3 (500 A), 850 N/m^3 (600 A) and 990 N/m^3 (700 A), respectively (volume force). These values are significantly larger than the values of F_L that can drive the motion of the melt, reported by Hou et al. [48] and Spitans et al. [49] (about 300 to 400 N/m^3), who demonstrated that the Lorentz force can drive the unidirectional rotation of the melt via numerical simulation. Additionally in the present study, this Lorentz force's presence should cause the slag pool's melt to generate a unidirectional flow in a lateral direction, as shown in Supplementary Video S2 and Figure 5c (top view of the slag pool). In addition to the two vertical flows mentioned above, there is a lateral circulating flow (unidirectional) in the slag pool after applying the ASMF. Consequently, the temperature distribution in the slag pool becomes more uniform, and heat transfer (Q_2) from liquid slag to metal pool becomes more uniform (Figure 5b). Applying the ASMF results in a more homogeneous temperature distribution and a shallower morphology for the metal pool, as shown in Figures 2 and 3b.

The heat transfer at the solid–liquid interface can also impact the temperature distribution in a metal pool. A temperature gradient $\bigtriangledown$T induces a Seebeck electromotive force S$\bigtriangledown$T for any material, where S denotes the material's thermoelectric power [50]. When a medium is subjected to a temperature gradient, a thermoelectric current (J_{TE}) can be generated. It is simple to understand why the temperature at the tip of a dendrite (in the mushy zone of an ESR ingot) is higher than its temperature at its base ($T_1 > T_2$ in Figure 5d). Thus, a non-isothermal interface and a J_{TE} will form between the dendrite and the liquid melt surrounding it (the yellow closed circle in Figure 5d). Previous research [51] discovered that a thermoelectric magnetic force (TEMF), created by the interaction of the J_{TE} and an external ASMF, can induce macroscopic unidirectional thermoelectric magnetic convection (TEMC), which would inevitably alter the heat transfer characteristics at the solid–liquid interface. Due to the interaction between J_{TEX} (the x-component of J_{TE}, yellow arrows) and the external ASMF, a macroscopic unidirectional TEMC is also presented in this study, as shown in Figure 5e (the top view of the metal pool). The existing TEMC can facilitate heat exchange at the front of solidification, thereby partially homogenizing the temperature distribution in the metal pool. This should be another reason for the shallower metal pool after applying ASMF.

The grain growth direction (in ESR) is known to be perpendicular to the solid–liquid interface of the metal pool, which is consistent with the results shown in Figure 2. Consequently, a NAGG region always exists in the central region of the LS, making the RFG region in the central region of the CS (i.e., the observed RFG is the cross section of the columnar grain, Figure 4). The ESR grains expands axially after applying the 50 mT ASMF (Figures 2 and 3b). Consequently, the width of the NAGG region widens, and the RFG is also distributed throughout the entire CS (after the addition of ASMF), as shown in Figures 3b and 4.

According to the analyses above, applying the 50 mT ASMF during the ESR process results in a shallower metal pool and axially growing grains. These modifications undoubtedly impact the formation and growth of ECs in electroslag remelted M2 HSS ingots, as will be discussed in more detail in the following section.

3.2. Refinement of ECs and Mechanisms

M_2C is a standard EC precipitated during the solidification of M2 HSS, which appears bright white in SEM-BSE images compared to the matrix due to its abundance of elements with higher atomic numbers such as W, Mo and V [12,52]. Other methods such as Mossbauer spectrometry are also effective (more convenient) in identifying carbides and matrix in steel, as reported by Siemiątkowski et al. [53]. Figure 6 illustrates the morphology of ECs in the C region of the ESR ingot under different experimental conditions. Absent the ASMF, the ECs exhibited a continuous network structure. Upon application of the ASMF, however, these structures became discontinuous (isolated or more uniformly distributed), as shown in Figure 6a–f. Based on the morphology difference, the ECs in Figure 6 can be primarily divided into two categories (with or without ASMF). One is a lamellar or feathery structure (red rectangles with dots), and the other is a maze or rod-like structure (green

dotted rectangles). In addition, some ECs and inclusions grew together, as shown by the yellow rectangles with dots in Figure 6.

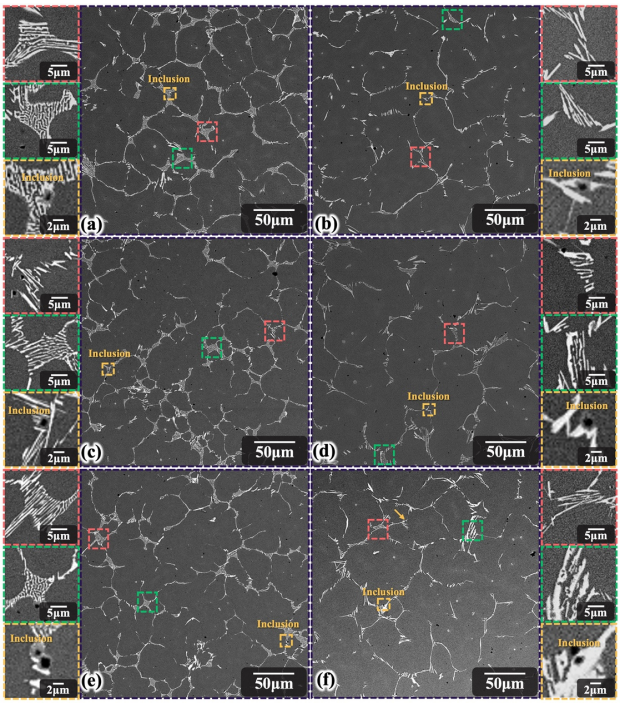


Figure 6. Morphology of ECs in C region of the ESR ingot under different experimental conditions, (**a**) 500 A 0 mT, (**b**) 500 A 50 mT, (**c**) 600 A 0 mT, (**d**) 600 A 50 mT, (**e**) 700 A 0 mT, (**f**) 700 A 50 mT, respectively.

The EDS results of two typical ECs (enlarged view) with different morphology and a unique structure (ECs grew together with inclusions) are shown in Figure 7. In abundance, two forms of ECs were discovered in W, Mo and V (Figure 7a,b). Moreover, Al_2O_3-(Ti, V)N was formed in association with the ECs, as shown in Figure 7c. According to Pervushin et al. [54], in the central region of (Ti, V)N, the oxide inclusion Al_2O_3 grew. The phenomenon was the heterogeneous nucleation of (Ti, V)N on Al_2O_3 during solidification, which was caused by a crystallographic relationship between TiN and oxide inclusions when the concept of planar lattice disregistry was utilized. This mechanism also explains why (Ti, V)N is wrapped by ECs in Figure 7c, where (Ti, V)N functions as heterogeneous nuclei for EC formation.

The area fractions of ECs in different regions (as well as the average value) of the ESR ingots under different experimental conditions are illustrated in Figure 8. After applying the ASMF, the ECs' average area fraction of ECs decreased marginally (Figure 8b). Apparently, in the absence of ASMF, the discrepancy in EC area fraction among the C, H and E regions was large, but this difference was significantly reduced after applying the ASMF (Figure 8a), indicating a more uniform distribution of ECs throughout the entire CS of the ESR ingot.

Figure 9 presents the statistical results of the size distribution of the ECs (600 A with or without ASMF) in this study. $d_{0.5}$ ($d_{0.9}$) reveals that 50% (90%) of the carbides are smaller than this value. Without ASMF, $d_{0.5}$ and $d_{0.9}$ were 12.26 μm and 27.29 μm, respectively; with ASMF, these values were reduced to 10.46 μm ($d_{0.5}$) and 18.51 μm ($d_{0.9}$). Therefore, applying the 50 mT ASMF benefited the EC's refinement.

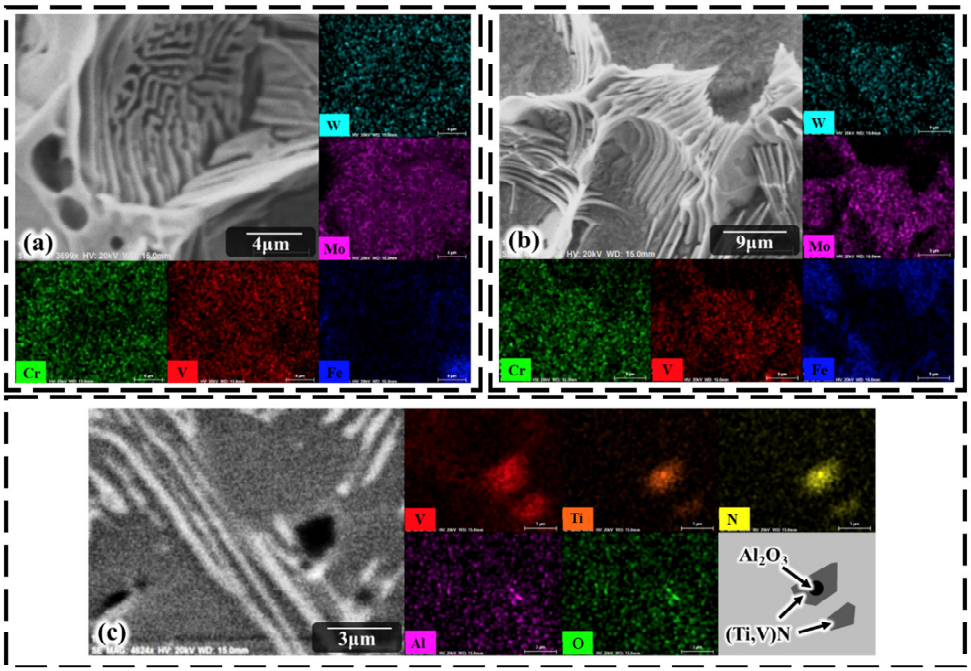


Figure 7. EDS results of the two typical ECs (enlarge view) with different morphology as well as the special structure (ECs grew together with inclusions). (**a**) Maze-like ECs, (**b**) Lamellar ECs, (**c**) ECs grew together with inclusions, respectively.

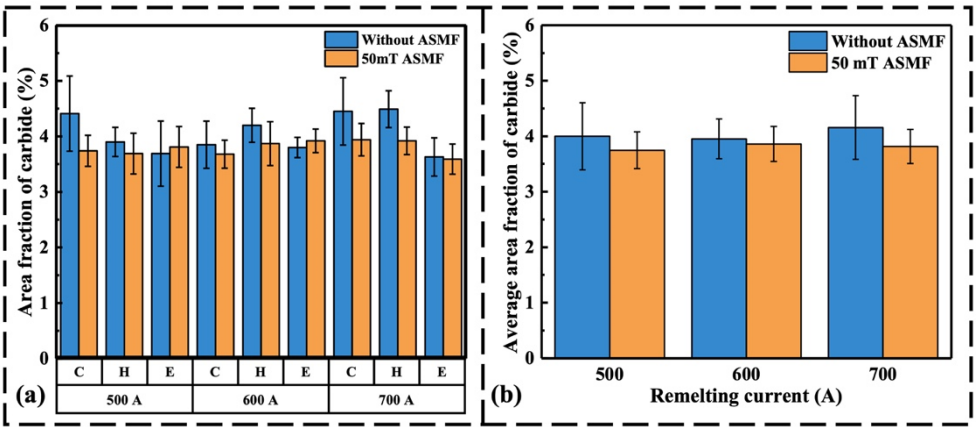


Figure 8. Area fraction of ECs in different regions (**a**) and the average value (**b**) of the ESR ingots under different experimental conditions.

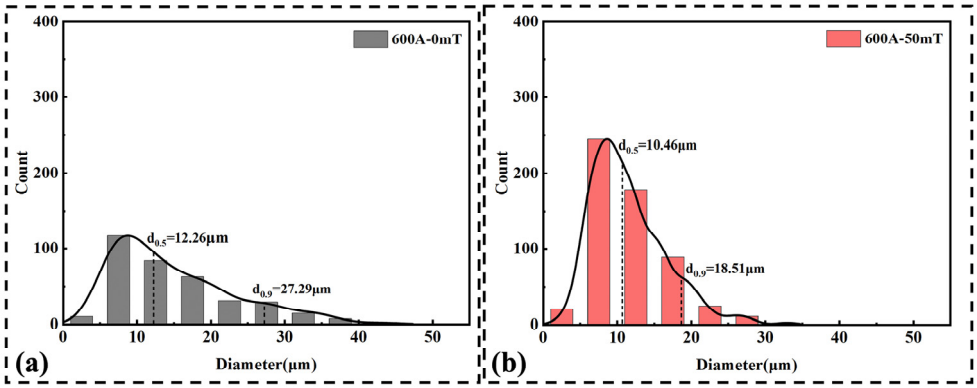


Figure 9. Statistical result of the size distribution of the ECs (600 A with or without ASMF) in this study. (**a**) 600A without ASMF, (**b**) 600A with ASMF, respectively.

The EBSD phase distribution and orientation of eutectic M_2C carbides (600 A with or without ASMF) are shown in Figure 10. Figure 10a(i),b(i) show the phase distribution of M_2C carbides, demonstrating once more that the application of ASMF is advantageous for eliminating coarse ECs. Additionally, it was discovered that different regions of the ECs structure have different crystallographic orientations in Figure 10a(ii),b(ii) (orientation of ECs), indicating that the EC structures observed in Figures 6 and 10 are formed by aggregating individual carbides. Figure 10a(iii),b(iii) exhibit the inverse pole figures of the crystallographic orientations (EC), which is often used to identify whether the crystallographic orientation of phase/grain is simple and varied [55]. It can be seen that more crystallographic orientation of the EC in the M2 HSS ESR ingot was obtained after the ASMF was applied, as shown in Figure 10a(iii),b(iii). These results (ECs morphology and orientation) show the same trend at 500 A and 700 A melting current conditions (with or without ASMF), and the related results can be found in Supplementary Figures S1 and S2, respectively.

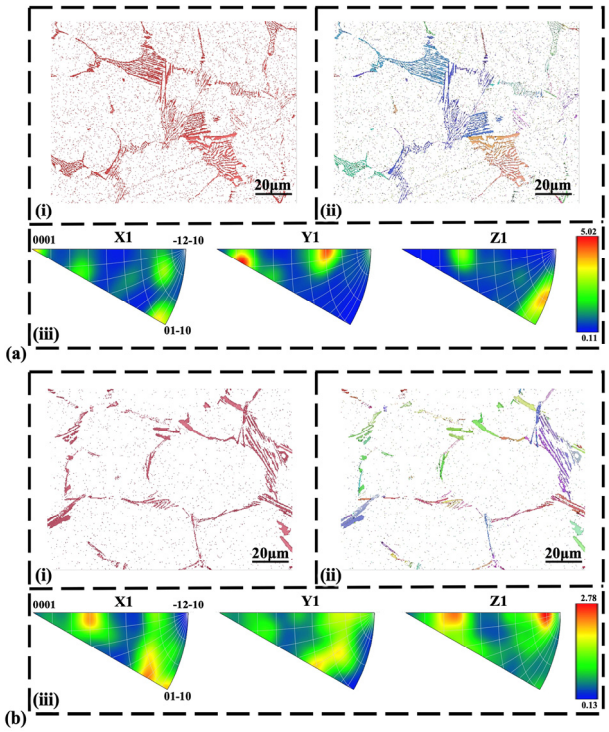


Figure 10. EBSD phase distribution and the orientation of eutectic M_2C carbides, (**a**) 600 A without ASMF, (**b**) 600 A with ASMF, respectively. (**i**) (**ii**) (**iii**) represent the phase distribution, crystallographic orientations and inverse pole figures of ECs in this study.

Numerous researchers [56,57] have studied the solidification process of M2 HSS. They pointed out that the inevitable redistribution of solute results in the segregation of carbide-forming elements (W, Mo, V and C) in the interdendritic region, which ultimately satisfies the conditions for eutectic reaction (L→γ + carbides) to occur at the solidification end of M2 HSS, leading to the formation of coarse ECs with continuous network morphology, as shown in Figure 6a,c,e. Due to the water-cooling effect of the sidewall of the mold, the E region of the ESR ingot solidified more rapidly. (The segregation degree decreased.) In this study, the area fraction of ECs was generally smaller in the E region than in the C and H regions (Figure 8a).

Figure 11 provides a schematic diagram of the formation of ECs in this research, with or without ASMF. Generally, there are two types of EC nucleation in M2 HSS [42]: non-heterogeneous nucleation (Figure 11a) and heterogeneous nucleation (Figure 11b). Carbide forming elements' concentration ([M] and [C] in Figure 11a) between dendrites for non-heterogeneous nucleation increases during solidification. Carbide (M_2C) is precipitated

as the primary precipitated phase when the conditions for a eutectic reaction are met. The iron required for austenite growth is then discharged from M_2C, and the carbide-forming elements necessary for its growth are absorbed from the austenite and residual melt. Afterwards, the EC is formed by alternating nucleation with austenite adjacent to it (Figure 11a), as reported by Zheng et al. [52] and Du et al. [58], who studied the formation characteristics of EC in M2 and similar M50 steel. In the case of heterogeneous nucleation, due to the presence of inclusions (typically Al_2O_3-(Ti,V)N in M2 HSS, Figure 7c), carbide also precipitates as the primary precipitated phase (with inclusions), and the subsequent alternating nucleation is similar to the case of non-heterogeneous nucleation, which eventually leads to the formation of EC (Figure 11b). It is evident from Figure 6 that both nucleation modes exist in this study, whether ASMF is applied.

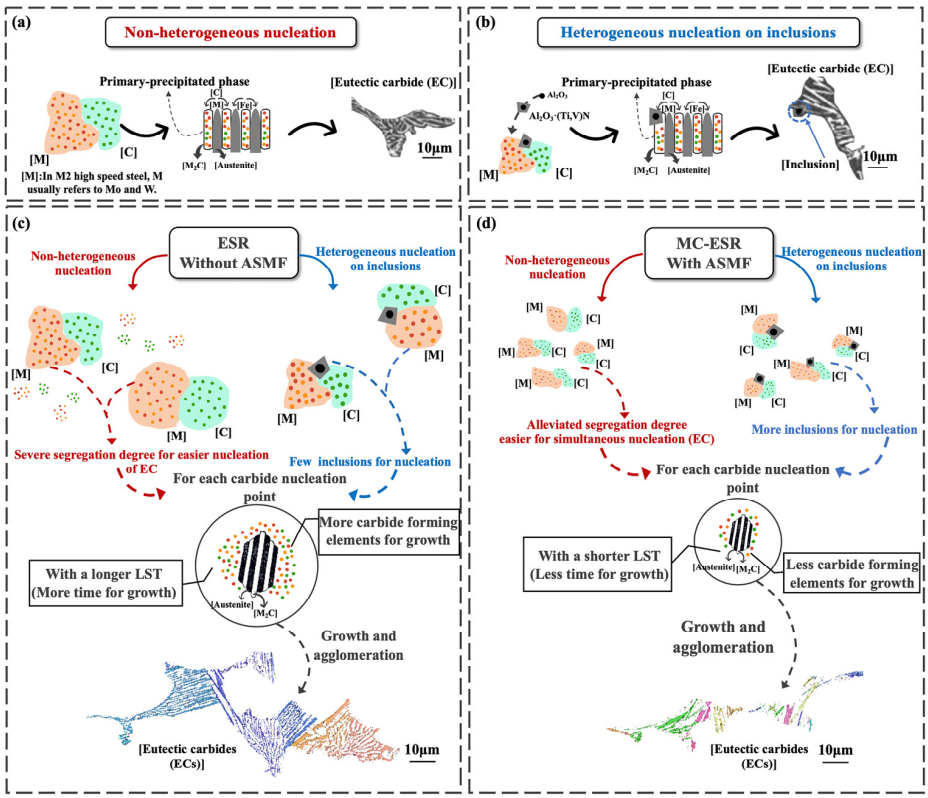


Figure 11. Schematic diagram of the ECs formation with or without ASMF in this study. (**a**) Non-heterogeneous nucleation of EC, (**b**) Heterogeneous nucleation of EC, (**c**) ECs formation without ASMF, (**d**) ECs formation with ASMF, respectively.

For non-heterogeneous nucleation, the segregation of carbide-forming elements in the interdendritic region has the greatest impact on the formation of EC. LST is a common value to evaluate the segregation degree, which represents the time that an alloy stays in the solid–liquid two-phase region (in mushy zone), which can be calculated using the following equations [24]. It is well established that lowering LST can alleviate the microsegregation degree.

$$LST = X_r / V \quad (1)$$

$$V = V_M \times \cos\theta \quad (2)$$

In Equation (1), X_r is the width of the mushy zone and V is the local solidification rate. In Equation (2), V_M is the rising velocity of the slag/metal pool interface (positively correlated with remelting rate) and θ is the angle between V_M and V, which is GGA defined in Figure 3. The schematic diagram of geometric relations (V_M, V, X_r and θ) during the ESR process are illustrated in Figure 12.

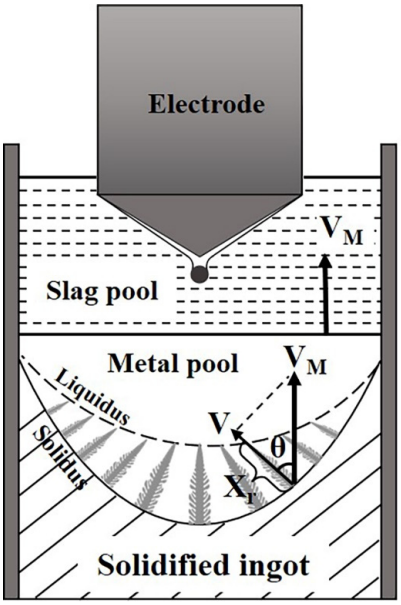


Figure 12. Schematic diagram of geometric relations (V_M, V, X_r and θ) during the ESR process.

From Equations (1) and (2), LST is dominated by X_r and V, while V is determined by V_M and GGA, respectively. It is assumed that the width of the mushy zone (X_r) was unchanged under the same remelting current conditions in this study. However, the value of GGA decreased (shallower metal pool) after applying the ASMF (Figure 3), leading to a larger cosθ. Meanwhile, because of the slightly increasing trend in the remelting rate described in the Experimentation part (Section 2.1), V_M in this study also increased due to ASMF. Therefore, faster local solidification rate and shorter LST (slight microsegregation in residual liquid) were obtained after the application of 50 mT ASMF (from Equations (1) and (2)). The degree of segregation in the interdendritic region decreased. As a result, the nucleation rate of EC increased (making simultaneous nucleation in different regions easier) due to larger undercooling degree, as shown in Figure 11c,d.

In the case of heterogeneous nucleation, inclusions in the residual liquid that serve as nucleation sites for EC nucleation (heterogeneous nucleation) could substantially decrease the required supersaturation for EC nucleation, thereby facilitating EC refinement [59]. Without ASMF, the corresponding numbers of (Ti, V)N-Al_2O_3 inclusions that acted as nuclei sites for EC formation were 394 (500 A), 402 (600 A) and 415 (700 A). (A total of 20 photos with the same magnification in Figure 6 were counted statistically.) These values, respectively, increased to 627, 680 and 667 after the ASMF was implemented, indicating that the effect of EC refinement by this factor increased (Figure 11c,d).

More significantly, in both non-heterogeneous and heterogeneous nucleation cases, ECs were formed through EC's subsequent growth and aggregation processes. Due to severe elemental segregation in the interdendritic region and longer LST, more carbide-forming elements and time were available for the growth of EC without ASMF, resulting in coarser ECs (Figures 9 and 11c). After ASMF was applied, the LST was shortened, and the segregation degree was reduced (less carbide-forming elements), both of which were detrimental to the growth of EC. Consequently, more refined ECs were obtained (Figures 9 and 11d). Moreover, the increase in the number of nucleation sites (both in non-heterogeneous and heterogeneous cases) resulted in the simultaneous nucleation and growth of EC, which should be a primary reason for the significant increase in the crystallographic orientation of EC after applying ASMF in this study, as shown in Figure 10a(iii),b(iii).

As described in Section 3.1, the Joule heat (temperature) distribution in the metal pool became more uniform after the 50 mT ASMF was implemented. The condition for the precipitation and growth of ECs in the entire region of the metal pool became more consistent than that without applying ASMF. It is consistent with the statistical result

depicted in Figure 8a, which indicates that after the application of the ASMF, the difference between the area fractions (ECs) of the C, H, and E regions of the ESR ingot shrunk. Due to the evenly distributed ECs, the hardness uniformity on the CS and LS of the ESR ingot improved, while standard deviations decreased (Supplementary Figures S3–S5), indicating that applying ASMF improved the homogeneity of M2 HSS ESR ingot.

4. Conclusions

This study investigates the effects of a superimposed ASMF on the morphology of metal pool and ECs in electroslag-remelted M2 HSS. Here are the principal conclusions:

1. Upon application of the 50 mT ASMF, the metal pool of the ESR ingot (M2 HSS, 60 mm diameter) became shallower (32.1 mm to 20.7 mm for 500 A; 38.2 mm to 25.9 mm for 600 A; 42.6 mm to 27.7 mm for 700 A, respectively), and the solidified structure exhibited an axial growth tendency (average GGA, 50.1° to 37.3° for 500 A; 52.7° to 41.6° for 600 A; 55.3° to 44.1° for 700 A, respectively). Lorentz force-driven unidirectional circulation in slag pool was the primary cause of the metal pool's morphological adjustment; this resulted in a more homogenous temperature distribution in slag pool. Thus, the heat transfer from the slag pool to the metal pool became more uniform, creating a metal pool that is shallower.
2. Due to ASMF, LST became shorter, while the number of (Ti, V)N-Al_2O_3 inclusions serving as heterogeneous nuclei for EC formation increased (394 to 627 for 500 A; 402 to 680 for 600 A; 415 to 667 for 700 A, respectively), yielding the formation of finer ECs ($d_{0.5}$: 12.26 μm to 10.46 μm; $d_{0.9}$: 27.29 μm to 18.51 μm, 600 A, respectively) with more crystallographic orientations in ESR ingots (M2 HSS).
3. Due to the uniformly distributed ECs (also refined), the hardness uniformity of the ESR ingot (M2 HSS, CS and LS) increased and standard deviations decreased (CS: 1.65 to 1.08 for 500 A, 1.39 to 1.18 for 600 A, 1.54 to 1.06 for 700 A; LS: 1.10 to 0.91 for 500 A, 1.08 to 0.94 for 600 A, 1.18 to 0.79 for 700 A, respectively), indicating that the ASMF facilitated the homogeneity of the ESR ingot (M2 HSS).

Supplementary Materials: The following supporting information can be downloaded at: https://www.mdpi.com/article/10.3390/met13050912/s1, Figure S1: EBSD phase distribution and the orientation of eutectic M2C carbides, (a) 500 A without ASMF, (b) 500 A with ASMF, respectively; Figure S2: EBSD phase distribution and the orientation of eutectic M2C carbides, (a) 700 A without ASMF, (b) 700 A with ASMF, respectively; Figure S3: Hardness (HRC) distribution on CS of the ESR ingot (M2 HSS) under different experimental conditions in this study, (a) 500 A without ASMF, (b) 500 A with ASMF, (c) 600 A without ASMF, (d) 600 A with ASMF, (e) 700 A without ASMF, (f) 700 A with ASMF, respectively. Figure S4: Hardness (HRC) distribution on LS of the ESR ingot (M2 HSS) under different experimental conditions in this study, (a) 500 A without ASMF, (b) 600 A without ASMF, (c) 700 A without ASMF, (d) 500 A with ASMF, (e) 600 A with ASMF, (f) 700 A with ASMF, respectively. Figure S5: Standard deviations (S. D.) of the hardness value (HRC) of the ESR ingot (M2 HSS) under different experimental conditions in this study, (a) on CS, (b) on LS, respectively. Video S1: Melt flow video of slag pool (600 A without ASMF); Video S2: Melt flow video of slag pool (600 A with ASMF).

Author Contributions: Data collection, X.Z.; data analysis, X.Z.; writing—original draft, X.Z. and Y.G.; Data interpretation, Z.S. (Zhonghao Sun) and Z.X.; Formal analysis, Z.S. (Zhonghao Sun), Z.X., C.L., Z.S. (Zhe Shen), B.D., Q.L., Y.Z. and T.Z.; Methodology, Z.S. (Zhonghao Sun). and Z.X.; Resources, C.L., Z.S. (Zhe Shen), B.D., Q.L., Y.Z. and T.Z.; Visualization, C.L., Z.S. (Zhe Shen), B.D. and T.Z.; Study design, Y.G.; Supervision, Y.G.; Funding acquisition, Y.G., Q.L. and Y.Z. All authors have read and agreed to the published version of the manuscript.

Funding: This research was funded by Young Elite Scientists Sponsorship Program by CAST (2022QNRC001), National Natural Science Foundation of China [52004156 and 52204347] and Science and Technology Commission of Shanghai Municipality (21SQBS00700). The APC was funded by National Natural Science Foundation of China [52004156 and 52204347].

Data Availability Statement: Data is contained within the article or supplementary material.

Acknowledgments: The authors gratefully acknowledged the financial support of the National Key Research and Development Program of China (2022YFC2904900), Changxu Innovation Center for Advanced Materials (SCXKFJJ202204).

Conflicts of Interest: The authors declare no conflict of interest.

References

1. Li, Y.; Wang, Y.; Niu, J.Z.; Liu, S.F.; Lin, Y.; Liu, N.; Ma, J.; Zhang, Z.H.; Wang, J. Microstructure and mechanical properties of M2 high speed steel produced by electron beam melting. *Mater. Sci. Eng. A* **2023**, *862*, 144327. [CrossRef]
2. Badisch, E.; Mitterer, C. Abrasive wear of high speed steels: Influence of abrasive particles and primary carbides on wear resistance. *Tribol. Int.* **2003**, *36*, 765–770. [CrossRef]
3. Leskovšek, V.; Ule, B.; Liščić, B. Relations between fracture toughness, hradness and microstructure of vacuum heat-treated high-speed steel. *J. Mater. Process. Technol.* **2002**, *127*, 308. [CrossRef]
4. Guo, J.; Ai, L.Q.; Wang, T.T.; Feng, Y.L.; Wan, D.C.; Yang, Q.X. Microstructure evolution and micro-mechanical behavior of secondary carbides at grain boundary in a Fe–Cr–W–Mo–V–C alloy. *Mater. Sci. Eng. A* **2018**, *715*, 359–369. [CrossRef]
5. Chaus, A.S.; Sahul, M.; Moravčík, R.; Sobota, R. Role of microstructural factor in wear resistance and cutting performance of high-speed steel end mills. *Wear* **2021**, *474–475*, 203865. [CrossRef]
6. Hanlon, D.N.; Rainforth, W.M. The rolling sliding wear response of conventionally processed and spray formed high speed steel at ambient and elevated temperature. *Wear* **2003**, *255*, 956–966. [CrossRef]
7. Chaus, A.S.; Hudáková, M. Wear resistance of high-speed steels and cutting performance of tool related to structural factors. *Wear* **2009**, *267*, 1051–1055. [CrossRef]
8. Chaus, A.S.; Bračík, M.; Sahul, M.; Dománková, M. Microstructure and properties of M2 high-speed steel cast by the gravity and vacuum investment casting. *Vacuum* **2019**, *162*, 183–198. [CrossRef]
9. Yin, D.M.; de Laat, B. Commentary on: Circulating plasmablasts contribute to antiphospholipid antibody production, associated with type I interferon upregulation. *J. Thromb. Haemost.* **2019**, *17*, 1030–1032. [CrossRef]
10. Luan, Y.K.; Song, N.N.; Bai, Y.L.; Kang, X.H.; Li, D.Z. Effect of solidification rate on the morphology and distribution of eutectic carbides in centrifugal casting high-speed steel rolls. *J. Mater. Process. Technol.* **2010**, *210*, 536–541. [CrossRef]
11. Zhou, X.F.; Fang, F.; Li, G.; Jiang, J.Q. Morphology and Properties of M2C Eutectic Carbides in AISI M2 Steel. *ISIJ Int.* **2010**, *50*, 1151–1157. [CrossRef]
12. Zhou, X.F.; Zhu, W.L.; Jiang, H.B.; Fang, F.; Tu, Y.Y.; Jiang, J.Q. A New Approach for Refining Carbide Dimensions in M42 Super Hard High-speed Steel. *J. Iron Steel Res. Int.* **2016**, *23*, 800–807. [CrossRef]
13. Alvarães, C.P.; Jorge, J.C.F.; Souza, L.F.G.d.; Araújo, L.S.; Mendes, M.C.; Farneze, H.N. Microstructure and corrosion properties of single layer Inconel 625 weld cladding obtained by the electroslag welding process. *J. Mater. Res. Technol.* **2020**, *9*, 16146–16158. [CrossRef]
14. Duan, S.C.; Shi, X.; Wang, F.; Zhang, M.C.; Li, B.; Yang, W.S.; Guo, H.J.; Guo, J. Investigation of desulfurization of Inconel 718 superalloys by ESR type slags with different TiO2 content. *J. Mater. Res. Technol.* **2019**, *8*, 2508–2516. [CrossRef]
15. Arh, B.; Podgornik, B.; Burja, J. Electroslag remelting: A process overview. *Mater. Technol.* **2016**, *50*, 971–979. [CrossRef]
16. Qiu, G.X.; Zhan, D.P.; Li, C.S.; Yang, Y.K.; Jiang, Z.H.; Zhang, H. Effects of electroslag remelting process and Y on the inclusions and mechanical properties of the CLAM steel. *Nucl. Eng. Technol.* **2020**, *52*, 811–818. [CrossRef]
17. Rao, L.; Zhao, J.H.; Zhao, Z.X.; Ding, G.; Geng, M.P. Macro- and Microstructure Evolution of 5CrNiMo Steel Ingots during Electroslag Remelting Process. *J. Iron Steel Res. Int.* **2014**, *21*, 644–652. [CrossRef]
18. Wang, Q.; Li, B.K. Numerical investigation on the effect of fill ratio on macrosegregation in electroslag remelting ingot. *Appl. Therm. Eng.* **2015**, *91*, 116–125. [CrossRef]
19. Dong, Y.W.; Jiang, Z.H.; Li, Z.B. Segregation of Niobium During Electroslag Remelting Process. *J. Iron Steel Res. Int.* **2009**, *16*, 7–11. [CrossRef]
20. Jardy, A.; Ablitzer, D. Mathematical modelling of superalloy remelting operations. *Mater. Sci. Technol.* **2013**, *25*, 163–169. [CrossRef]
21. Gao, J.G.; Yang, S.L.; Zhao, P.; Yang, S.F.; Li, J.S.; Liu, W.; Zhang, C.L. Optimization of Process Parameters for ESR Waspaloy Superalloy by Numerical Simulation. *Materials* **2022**, *15*, 7483. [CrossRef] [PubMed]
22. Liu, Q.X.; Lu, D.P.; Lu, L.; Hu, Q.; Fu, Q.F.; Zhou, Z. Effect of Mischmetal on As-cast Microstructure and Mechanical Properties of M2 High Speed. *J. Iron Steel Res. Int.* **2015**, *22*, 245–249. [CrossRef]
23. Yin, F.X.; Wang, L.; Xiao, Z.X.; Feng, J.H.; Zhao, L. Effect of titanium and rare earth microalloying on microsegregation, eutectic carbides of M2 high speed steel during ESR process. *J. Rare Earths* **2020**, *38*, 1030–1038. [CrossRef]
24. Du, G.; Li, J.; Wang, Z.B. Control of Carbide Precipitation During Electroslag Remelting-Continuous Rapid Solidification of GCr15 Steel. *Metall. Mater. Trans. B* **2017**, *48*, 2873–2890. [CrossRef]
25. Yu, W.T.; Li, J.; Shi, C.B.; Zhu, Q.T. Effect of Electroslag Remelting Parameters on Primary Carbides in Stainless Steel 8Cr13MoV. *Mater. Trans.* **2016**, *57*, 1547–1551. [CrossRef]
26. Chang, L.Z.; Shi, X.F.; Yang, H.S.; Li, Z.B. Effect of Low-Frequency AC Power Supply During Electroslag Remelting on Qualities of Alloy Steel. *J. Iron Steel Res. Int.* **2009**, *16*, 7–11. [CrossRef]

27. Cao, H.B.; Jiang, Z.H.; Dong, Y.W.; Liu, F.B.; Cao, Y.L.; Hou, Z.W.; Yao, K.A.; Xu, M.X. Effect of Single Power Two Circuits Electroslag Remelting Process on the Ingot Solidification Quality. *Steel Res. Int.* **2018**, *90*, 1800337. [CrossRef]
28. Chumanov, I.V.; Matveeva, M.A.; Sergeev, D.V. Influence of Electrode Rotation in Electroslag Remelting on the Anisotropy of Ingot Properties. *Steel Transl.* **2019**, *49*, 77–81. [CrossRef]
29. Chen, J.S.; Chang, K.H.; Zheng, F.Z.; Zhang, Z.; Chang, L.Z. Effect of electroslag remelting mould rotation on solidification process of M2 high speed steel. *Chin. J. Process Eng.* **2019**, *19*, 581–588.
30. Chang, L.Z.; Chang, K.H.; Zhu, X.M.; Chen, J.S.; Gao, G. Effect of mould rotation on inclusions in ESR ingot. *Chin. J. Process Eng.* **2019**, *19*, 1186–1196.
31. Qi, Y.F.; Li, J.; Shi, C.B.; Zhang, Y.; Zhu, Q.T.; Wang, H. Effect of directional solidification of electroslag remelting on the microstructure and primary carbides in an austenitic hot-work die steel. *J. Mater. Process. Technol.* **2017**, *249*, 32–38. [CrossRef]
32. Qi, Y.F.; Li, J.; Shi, C.B.; Wang, H.; Zheng, D.L. Precipitation and growth of MnS inclusion in an austenitic hot-work die steel during ESR solidification process. *Metall. Res. Technol.* **2019**, *116*, 322. [CrossRef]
33. Li, F.L.; Fu, R.; Feng, D.; Yin, F.J.; Tian, Z.L. Microstructure and Segregation Behavior of Rene88DT Alloy Prepared by ESR-CDS. *Rare Metal Mater. Eng.* **2016**, *45*, 1437–1442. [CrossRef]
34. Qi, Y.F.; Li, J.; Shi, C.B.; Geng, R.M.; Zhang, J. Effect of Directional Solidification in Electroslag Remelting on the Microstructure and Cleanliness of an Austenitic Hot-work Die Steel. *ISIJ Int.* **2018**, *58*, 1275–1284. [CrossRef]
35. Guo, Y.F.; Xia, Z.B.; Shen, Z.; Li, Q.; Sun, C.X.; Zheng, T.X.; Ren, W.L.; Lei, Z.S.; Zhong, Y.B. Enhancement of removing inclusions from liquid melt film during the ESR process assisted by a static magnetic field. *J. Mater. Process. Technol.* **2021**, *290*, 116962. [CrossRef]
36. Mitchell, A.; Hernandez-Morales, B. Electromagnetic stirring with alternating current during electroslag remelting. *Metall. Trans. B* **1990**, *21*, 723–731. [CrossRef]
37. Wang, Q.; Yan, H.G.; Wang, F.; Li, B.K. Impact of Electromagnetic Stirring on Grain Structure of Electroslag Remelting Ingot. *JOM* **2015**, *67*, 1821–1829. [CrossRef]
38. Zhong, Y.B.; Li, Q.; Fang, Y.P.; Wang, H.; Peng, M.H.; Dong, L.C.; Zheng, T.X.; Lei, Z.S.; Ren, W.L.; Ren, Z.M. Effect of transverse static magnetic field on microstructure and properties of GCr15 bearing steel in electroslag continuous casting process. *Mater. Sci. Eng. A* **2016**, *660*, 118–126. [CrossRef]
39. Li, Q.; Xia, Z.B.; Guo, Y.F.; Shen, Z.; Zheng, T.X.; Zhong, Y.B. Microstructure Evolution and Mechanical Properties Improvement in Magnetic-controlled Electroslag Remelted Bearing Steel. *ISIJ Int.* **2020**, *60*, 2462–2470. [CrossRef]
40. Ma, C.K.; Xia, Z.B.; Guo, Y.F.; Liu, W.F.; Zhao, X.H.; Li, Q.; Qi, W.T.; Zhong, Y.B. Carbides refinement and mechanical properties improvement of H13 die steel by magnetic-controlled electroslag remelting. *J. Mater. Res. Technol.* **2022**, *19*, 3272–3286. [CrossRef]
41. Ma, C.K.; Deng, G.D.; Sun, Z.H.; Zheng, T.X.; Shen, Z.; Ding, B.; Liu, C.M.; Guo, Y.F.; Li, Q.; Zhong, Y.B. Cleanliness improvement and microstructure refinement of H13 die steel by laboratory magnetic-controlled electroslag remelting. *J. Mater. Res. Technol.* **2023**, *24*, 2086–2099. [CrossRef]
42. Guo, Y.F.; Qi, W.T.; Xia, Z.B.; Zhao, X.H.; Li, Q.; Liu, C.M.; Ding, B.; Shen, Z.; Zheng, T.X.; Zhong, Y.B. Morphology tailoring of metal pool and eutectic carbides in magnetic-controlled electroslag remelted M2 high-speed steel. *J. Mater. Res. Technol.* **2022**, *16*, 1122–1135. [CrossRef]
43. Guo, Y.F.; Qi, W.T.; Xia, Z.B.; Lin, W.H.; Liu, C.M.; Shi, P.J.; Li, Q.; Shen, Z.; Ding, B.; Zheng, T.X.; et al. Refinement of Eutectic Carbides in M2 High Speed Steel by Adjusting Magnetic Flux Density During Magnetic Controlled ESR Process. *Metall. Mater. Trans. B* **2022**, *53*, 3384–3395. [CrossRef]
44. Wang, H.; Zhong, Y.; Li, Q.; Li, W.; Ren, W.; Lei, Z.; Ren, Z.; He, Q. Influences of the Transverse Static Magnetic Field on the Droplet Evolution Behaviors during the Low Frequency Electroslag Remelting Process. *ISIJ Int.* **2017**, *57*, 2157–2164. [CrossRef]
45. Wang, Q.; Yan, H.G.; Ren, N.; Li, B.K. Effect of current on solute transport in electroslag remelting dual alloy ingot. *Appl. Therm. Eng.* **2016**, *101*, 564–567. [CrossRef]
46. Li, Z.B. *Electroslag Metallurgy Theory and Practice*; Metallurgical Industry Press: Beijing, China, 2010; pp. 21–25.
47. Li, Q.; Zhong, Y.B.; Sun, C.X.; Wang, H.; Zheng, T.X.; Ren, W.L.; Ren, Z.M. Effect of Transverse Static Magnetic Field on Droplets Transient and Inclusions Evolution During the Electroslag Remelting Process of GCr15 Ingots. *Acta Metall. Sin.* **2018**, *31*, 1311–1316. [CrossRef]
48. Hou, Z.W.; Dong, Y.W.; Jiang, Z.H.; Hu, Z.H.; Liu, L.M.; Tian, K.J. Effect of an external magnetic field on improved electroslag remelting cladding process. *Int. J. Miner. Metall. Mater.* **2022**, *29*, 1511–1521. [CrossRef]
49. Spitans, S.; Franz, H.; Scholz, H.; Reiter, G.; Baake, E. Numerical simulation of the ingot growth during the vacuum arc remelting process. *Magnetohydrodynamics* **2017**, *53*, 557–569.
50. Shen, Z.; Zhou, B.F.; Zhong, Y.B.; Dong, L.C.; Wang, H.; Fan, L.J.; Zheng, T.X.; Li, C.J.; Ren, W.L.; Xuan, W.D.; et al. An Electromagnetic Compounding Technique for Counteracting the Thermoelectric Magnetic Effect During Directional Solidification Under a Transverse Static Magnetic Field. *Metall. Mater. Trans. A* **2018**, *49*, 3373–3382. [CrossRef]
51. Zheng, T.X.; Zhong, Y.B.; Wang, J.; Ren, Z.M.; Ren, W.L.; Lei, Z.S.; Debray, F.; Beaugnon, E.; Wei, X.C. Droplet Evolution and Refinement During Liquid–Liquid Decomposition of Zn-6 Wt Pct Bi Immiscible Alloy Under High Static Magnetic Fields. *Metall. Mater. Trans. A* **2018**, *49*, 3333–3345. [CrossRef]

52. Zheng, T.X.; Li, W.Q.; Qi, W.T.; Xia, Z.B.; Li, Q.; Shen, Z.; Guo, Y.F.; Zhong, Y.B.; Wang, H.; Wang, Q.L. Morphology transition of eutectic carbide assisted by thermoelectric magnetic force during the directional solidification of M2 high-speed steel. *Ironmak. Steelmak.* **2021**, *48*, 885–892. [CrossRef]
53. Siemiątkowski, Z.; Szumiata, T.; Gzik-Szumiata, M.; Martynowski, R.; Rucki, M. Application of the microscopic and Mössbauer studies to the analysis of a marine diesel engine crankshaft. *J. Mar. Eng. Technol.* **2018**, *17*, 160–167. [CrossRef]
54. Pervushin, G.V.; Suito, H. Effect of primary deoxidation products of Al_2O_3, ZrO_2, Ce_2O_3 and MgO on TiN precipitation in Fe-10mass%Ni alloy. *ISIJ Int.* **2001**, *41*, 748–756. [CrossRef]
55. He, A.N.; Li, J.W.; Wang, M.K.; Wang, A.D.; Xiao, Y.; Dong, Y.Q.; Guo, H.; Jiang, R.R.; Xia, W.X.; Dong, L.H.; et al. Microstructure, magnetic domain and dynamic loss of surface-textured Fe-based nanocrystalline alloy. *J. Mater. Sci. Technol.* **2022**, *120*, 1–7. [CrossRef]
56. Wieczerzak, K.; Bala, P.; Stepien, M.; Cios, G.; Koziel, T. Formation of eutectic carbides in Fe–Cr–Mo–C alloy during non-equilibrium crystallization. *Mater. Des.* **2016**, *94*, 61–68. [CrossRef]
57. Guo, J.; Liu, S.; Zhou, Y.F.; Wang, J.B.; Xing, X.L.; Ren, X.J.; Yang, Q.X. Stability of eutectic carbide in Fe-Cr-Mo-W-V-C alloy. *Mater. Lett.* **2016**, *171*, 216–219. [CrossRef]
58. Du, N.; Liu, H.; Cao, Y.; Fu, P.; Sun, C.; Liu, H.; Li, D. Formation mechanism of MC and M_2C primary carbides in as-cast M50 bearing steel. *Mater. Charact.* **2021**, *174*, 111011. [CrossRef]
59. Zhang, J.; Li, J.; Shi, C.B.; Huang, J. Growth and agglomeration behaviors of eutectic M7C3 carbide in electroslag remelted martensitic stainless steel. *J. Mater. Res. Technol.* **2021**, *11*, 1490–1505. [CrossRef]

Disclaimer/Publisher's Note: The statements, opinions and data contained in all publications are solely those of the individual author(s) and contributor(s) and not of MDPI and/or the editor(s). MDPI and/or the editor(s) disclaim responsibility for any injury to people or property resulting from any ideas, methods, instructions or products referred to in the content.